



CPFD Simulation of Gas-Solid Flow in Dense Phase Zone of Pant-Leg Fluidized Bed with Secondary Air

H. P. Liu^{1†}, Y. Bi¹, H. W. Sun¹, L. Zhang², F. Yang¹ and Q. Wang¹

¹ Engineering Research Centre of Oil Shale Comprehensive Utilization, Ministry of Education, School of Energy and Power Engineering, Northeast Electric Power University, Jilin 132012, Jilin Province, China

² Department of Chemical & Biological Engineering, University of British Columbia, Vancouver, V6T1Z3, Canada

†Corresponding Author Email: hongpeng5460@126.com

(Received February 13, 2022; accepted May 16, 2022)

ABSTRACT

Aggregation of fluidization media may appear at the dense phase region of the pant-leg fluidized bed near the incline walls. When the particles flow along the inclined wall, the friction and drag force will cause the particles to accumulate on the inclined wall, resulting in an uneven distribution of particles. The stagnant zones can be minimized by correctly arranging secondary air. Computational particle fluid dynamics (CPFD) method was used to simulate the gas-solid two-phase flow pattern in the dense phase region of pant-leg fluidized bed. Cold tests were performed on a benchtop pant-leg fluidized bed. A high speed imaging technology was used to monitor the flow pattern in the dense phase area, whereas the bubble size and residence time were compared to verify the accuracy of the simulation. The gas-solid flow patterns under various models were simulated. The influence of different secondary air velocities on the reduction of stagnant zone in the dense phase zone of the fluidized bed were predicted. The results indicated that the introduction of secondary air could effectively promote the mixing of particles, and weaken the accumulation of particles on the inclined wall surface. Moreover, secondary air can effectively promote the flow between the gas-solid two-phases and improve the combustion characteristics in the furnace.

Keywords: Fluidized bed; Dense phase zone; Gas-solid flow; Numerical simulation; Secondary air; CPFD.

NOMENCLATURE

D	drag coefficient	u_g	gas phase velocity
F	gas phase macroscopic stress tensor	u_p	particle velocity
g	gas	ρ	density
g	acceleration due to gravity	τ_p	particle normal stress
p	particle	τ	momentum exchange rate
P_s	material parameter	θ_p	volume fraction of the particles
P	gas phase pressure	β	model's own parameters
t	time		

1. INTRODUCTION

The concept of fluidized bed first appeared in the field of chemical industry. In the late 1960s, circulating fluidized bed officially entered the stage of industrial application. As a clean and efficient combustion technique, circulating fluidized bed boiler has been largely used in power generation and petroleum refinery (for example fluidized catalytic crackers). It has the advantages of high fuel

flexibility, high combustion efficiency and low pollutant emissions (Basu 2015). The gas-solid properties have significant impact on the structural design and actual operation of circulating fluidized bed reactors. Many scholars have conducted extensive research on the gas-solid properties through experimental analysis and numerical simulations. At present, the models used in the gas-solid two-phase numerical simulations are the Euler-Eulerian calculation model and the Euler-Lagrange calculation model.

The Euler-Eulerian model calculates the state of flow field by solving a time-averaged Navier-Stokes equation and calculates a significant number of particles in the flow field. Both the gas and solid particles are treated as a continuous media, and the model is also known as the two-fluid model (Kleinstreuer 2003; Yeoh and Tu 2019). However, in the two-fluid model, the solid phase can only be set to a single particle size, which does not represent the broad sieving characteristics of actual particles (Gao *et al.* 2008; Jenkins and Mancini 1989). Grace and Sun (1991) pointed out that the particle size distribution could obviously affect the operation performance of fluidized bed reactors.

The Euler-Lagrange model considers gas as a continuous medium. In this model, the Discrete Element Method (DEM), proposed by Cundall and Strack (1979), is applied. However, in the current Lagrange calculations, the complex particle conditions limit the number of particles (Godlieb *et al.* 2007; O'Rourke 1981; Snider *et al.* 2011) for which, the model can be solved. At present, computational power limits the number of particles for which the model can be solved up to 10^6 (Hartge *et al.* 2009), while the number of particles in real situations can be significantly higher than this.

The computational particle fluid dynamics (CPFD) model is a novel Euler-Lagrange model, in which the fluid uses a coupled Navier-Stokes (N-S) equation between discrete parts. The particle momentum model is based on the multiphase particle-in-cell (MP-PIC) numerical description (Snider 2001; Snider *et al.* 1998). The calculation switches between the Euler system and the Lagrange system. This switching is different from the coupling of the two solvers of the discrete element method. The CPFD model considers the huge difference between the particles and fluids in detail, and truly deals with the motion characteristics of particles. The model avoids the time-consuming particle contact retrieval and uses the well-established particle dynamics theory to compute the interparticle interactions. The CPFD model proposes the concept of computational granules, which treats particles as micro clusters based on the concept of basic fluid micelles of the Lagrange method. In other words, multiple real particles are considered as a single calculated particle, which has the same material properties and physical motions. Shi *et al.* (2014, 2015) found that the CPFD method could effectively predict the hydrodynamic parameters, the average residence time of solids and the particle size distribution. Similarly, Chen *et al.* (2013) investigated the feasibility of using CPFD model to simulate the particle size distribution in a circulating fluidized bed boiler and pointed out that the results from CPFD model were more accurate than the traditional two-fluid model. Liu *et al.* (2017) investigated the lamination characteristics of circulating fluidized bed under different bed material heights using the CPFD method. Qiu *et al.* (2015) presented a new type of annular combustion chamber to enhance the secondary air penetration in circulating fluidized bed (CFB). The gas-solid

flow characteristics were studied and the structure of annular combustion chamber was optimized. It was shown that the gas-solid flow in the annular combustion chamber was similar to that in the conventional CFB riser. Abbasi *et al.* (2011) performed CPFD simulation on the feed section of the fast fluidized bed gasifier. The results supported that the two-dimensional CPFD model could effectively predict the flow pattern of particles near the feed zone. Nardo *et al.* (2018) found that CPFD model could assure a more effective contact of gas with solid bed and a good bubbling fluidization mechanism, and the prediction of the outlet gas composition was satisfactory. Raheem *et al.* (2019) conducted experimental and CPFD numerical research on CFB combustor under cold flow conditions. The simulation results of the two drag models agreed well with the experimentally measured results (<5%), and energy minimization multi-scale (EMMS) could predict the pressure distribution more accurately than the Wen-Yu/Ergun model. Yan *et al.* (2020) conducted combustion simulations on a 600 MW supercritical CFB boiler using the CPFD method and proposed a new method to estimate the distributions of coal supply. Zhang and Li (2020) numerically studied the gas - solid flow behavior in a high density circulating fluidized bed riser using the CPFD method. The exit geometry was found to distinctly affect the axial distribution of the solid volume fraction throughout the riser. On the basis of MP-PIC method, Cui and Zhong (2021) conducted a numerical study on the amplification characteristics and regularities of the S-CO₂ CFB boiler with increased boiler power capacity. Based on the MP-PIC method, Tu and Luo (2021) conducted computational fluid dynamics simulation on the laboratory-scale cold three-dimensional full loop double fluidized bed model to study its gas-solid two-phase flow characteristics. MP-PIC belongs to the coarse particle method, which has the struggles to confirm the appropriate coarse particle size. However, the number of particles to be tracked can be greatly reduced. Under reasonable parameters, similar results can be obtained using the discrete particle method. Nevertheless, the calculation speed can be a hundred times faster. It is a general trend to use the coarse particle method to simulate the gas-solid two-phase flow in industrial equipment.

Pant-leg fluidized bed has been widely used in large-scale CFB units due to enhanced penetration of secondary air at the dense bed region. While the volume of the dense bed region in the circulating fluidized bed accounts for a small portion of the entire furnace, the gas-solid mixing in the dense phase affects the performance of entire boiler. There are secondary air outlets, return ports and feed ports that are closer to the air distribution plate in the dense phase area. The gas-solid flow condition is complicated. Past research mainly focused on the traditional symmetrical structure of the dense phase area. With regards to the pant-type fluidized bed, studies have extensively investigated the bed overturn mechanism in pant-leg CFB, whereas limited research has analyzed

the mass transfer along the inclined wall and the arrangement of secondary air outlets to avoid the uneven mixing.

The aim of this study is to perform an experimental and numerical investigation into the influence of pant-leg structure and secondary air on the solids' distribution around the pant-leg structure in two-dimensional perspective. To the best of our knowledge, this is the first study applying CPFD simulation to explore the hydrodynamics at pant-leg structure in a CFB system, which is a significant aspect when scaling up the CFB to large commercial scale. By comparing the simulation results with the experimental results, the reliability of the model was verified. Moreover, the CPFD model was applied to predict the gas and solid flow patterns with the introduction of secondary air at different gas velocities. The improvement of solid and gas mixing at the leaning surface was discussed. Suggestions for the arrangement of secondary air outlets were also made.

Particle aggregation phenomenon was observed without the application of secondary air. The effect of primary air's velocity, secondary air's velocity and the static bed height on the sand flow pattern at the dense phase zone was investigated in the study. In addition, changes in the flow structure in the dense phase zone, caused by the addition of secondary air, were predicted. The purpose of the study was to improve the pant-leg fluidization of the particles by analyzing the particle aggregation in the fluidized bed and making the particle distribution more uniform.

2. EXPERIMENTAL SETUP

Limited by the experimental conditions, it was impossible to obtain the test data of industrial units. Therefore, a visual benchtop pant-leg structured fluidized bed was built based on the similarity method. The study object was a commercial 300MW pant-leg fluidized bed, and the scale proportion was 1:80. It can be referenced in practical operations. The benchtop pant-leg fluidized bed reactor was transparent and made of polymethyl methacrylate, as shown in Fig. 1. The height of the reactor was 456 mm. The cross-section of the furnace was 188 mm × 10 mm. The lower part of the furnace was a pant-leg structure with two air distributor plates. The dimensions of the air distribution plate were 44 mm × 10 mm. Two legs met at the height of 109 mm from the air distribution plates. The angle between the inclined wall of the leg and the horizontal plane was 65°.

Because the particle size, shape and density of quartz sand are close to that of coal ash, and its shape is similar, it will not be broken into fluidization. Therefore, quartz sand was applied as the bed material. The mean particle diameter of the bed material was 0.59 mm. The true density was 2565 kg/m³. The bulk density was 1760 kg/m³. The minimum fluidization velocity was 0.45 m/s. The particle size distribution of the bed material is presented in Table 1.

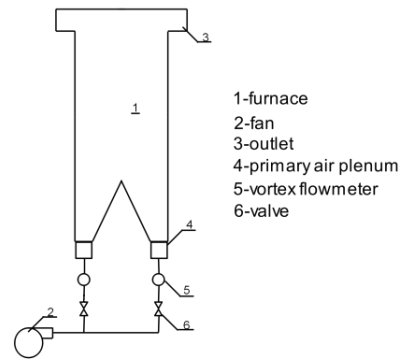


Fig. 1. Schematic of the test system.

Table 1 Particle size distribution

Particle size (mm)	Cumulative (%)
0.37 - 0.49	10
0.49 - 0.62	40
0.62 - 0.73	40
0.73 - 0.81	10

The bubble formation was studied in the dense phase of the fluidized bed of the side slanting wall. The fluidized air volume gradually increased from 0 to 5.5 m³/h, and the static bed height was varied through values of 20 mm and 55 mm in two separate tests. The particles in the dense phase region were moved from the bubbling state to the circulating fluidization state, and the bubble motion in the fluidized bed was recorded with high-speed imaging technology.

Because the light could not penetrate the particles in the bed, only the two-dimensional velocity field of particles could be measured in the dense phase area. This required that the thickness of the fluidized bed test bed be small enough to accurately reflect the two-dimensional flow characteristics. However, if the thickness of the test bed was too small, the accuracy of particle movement in the fluidized bed could not be guaranteed. After analyzing and summarizing the previous work, the bed thickness of the test-bed was determined to be 10 mm. The DC lamp with moderate brightness was used for illumination.

The vortex flowmeter (WYLU model), produced by Shanghai Wangyuan Company, China, was used as the fluidized air flow measurement device. When measuring the gas flow, the accuracy level of the vortex flowmeter was set to be 1.5%.

The particle image velocimetry (PIV) system was produced by the American TSI company. It had the features of high-precision measurement, online observation, and a variety of algorithms. Moreover, the pictures recorded by the high-speed camera were processed by the image processing software, Insight 3G. PIV overcomes the limitations of spatial single-point measurement technology and does not interfere with the flow field. It can record all the information of the measurement plane at a certain time. The image acquisition routine was as follows. Firstly, the equipment was checked. The laser was turned on, and the flow field position and laser

energy were adjusted. Then, the Insight 3G software was started, and the parameters were set. The target disk was calibrated, the appropriate brightness adjusted, and the image acquisition was carried out.

3. CPF D MODEL

3.1 Computational Geometry

Firstly, the geometric model of the calculation area was established and meshed. The mesh density distribution had a great impact on the numerical precision and real-time simulation. Considering the computational cost and the calculation accuracy, the distribution of the uniform mesh density was used (Atsonios *et al.*, 2011). The mesh was encrypted in the dense phase region of the lower part of the furnace. Then, the calculation conditions, boundary conditions and the selection of drag model were determined in the CPF D model. Finally, the calculated results were processed. The volume fraction of the particles of dense phase region, the velocities of the particles, and the velocity of gas were obtained. After meshing, physical properties of gas and solid were set. Normal-wall momentum retention and tangential-wall momentum retention were based on the Barracuda user manual (CPF D Software, 2015). The set parameters are presented in Table 2. To simplify the uniform distribution of primary air, only the primary air velocity was considered, and the starting point of the particle phase velocity was set to be 0 m/s. With regards to the numerical simulation calculation of gas-solid flow, since convergence is not necessary for CPF D, the calculation time of each working condition was 10 s.

Table 2 Simulation parameters

Gas density, ρ_g (kg/m ³)	1.2045
Solid density, ρ_s (kg/m ³)	1760
Sphericity	0.8
Normal-wall momentum retention	0.3
Tangential-wall momentum retention	0.99
Time step (s)	0.01

The influence of secondary air on the gas-solid two-phase flow in the dense phase region was analyzed using numerical simulation. Fig. 2 shows the geometric model and grid division diagram of the test bench with secondary air ports. There were six secondary air injection points located in the dense phase region, whereas the angle between the secondary air outlet and the horizontal direction was 30° (slanted down into the furnace). The secondary air outlet had a radius of 5 mm.

3.2 Governing Equations

The following equations can be used to obtain the variation pattern and parameters of particle motion. The main governing equations involved in the CPF D model are the gas-phase continuous equation in a gas-solid two-phase flow.



Fig. 2. Schematic of the geometric model and meshing.

$$\frac{\partial \theta_g \rho_g}{\partial t} + \nabla(\theta_g \rho_g u_g) = 0 \quad (1)$$

where ρ_g is the gas phase density, u_g is the gas phase velocity, and θ_g is the volume fraction of the gas phase.

The gas phase momentum equation is given by Eq. (2).

$$\frac{\partial \theta_g u_g}{\partial t} + \nabla(\theta_g \rho_g u_g) = -\frac{1}{\rho_g} \nabla P - \frac{1}{\rho_g} F + \theta_g g + \frac{1}{\rho_g} \nabla \tau \quad (2)$$

where P is the gas phase pressure, F is the gas phase macroscopic stress tensor, and τ is the momentum exchange rate of the gas phase and the particle phase per unit volume. Moreover, the parameter F is calculated using Eq. (3).

$$F = \iiint f V_p \rho_p \left[D(u_g - u_p) - \frac{1}{\rho_p} \nabla P \right] dV_p d\rho_p du_p \quad (3)$$

The momentum equation of the particle phase is given by Equation (4).

$$\frac{du_p}{dt} = D(u_g - u_p) - \frac{1}{\rho_p} \nabla P + g - \frac{1}{\theta_p \rho_g} \nabla \tau_p \quad (4)$$

where u_p is the particle velocity, ρ_p is the particle density, and τ_p is the particle normal stress.

Equation (4) characterizes the acceleration produced by the combination of aerodynamic drag, pressure gradient, gravity and normal stress gradient between the particles. In each cell, the volume fraction of the particles is given by Eq. (5).

$$\theta_p = \iiint f V_p dV_p d\rho_p du_p \quad (5)$$

Particle normal stress model is given by Eq. (6).

$$\tau = \frac{P_s \theta_p^\beta}{\max[(\theta_{cp} - \theta_p), \varepsilon(1 - \theta_p)]} \quad (6)$$

where P_s is the material parameter, $2 < \beta < 5$ is the model's own parameters (Auzerais *et al.* 1988), θ_{cp} is the volume fraction when the particles are closely packed, and ε is the small amount constructed to eliminate the singular points in the model solution (Snider 2001).

3.3 Drag Model

The addition of drag force model can reflect the changes in drag force during particle motion. The Wen-Yu model is limited to a particle volume fraction of 0.01 - 0.61 (Wen and Yu1966), while the Ergun equation is generally applicable within the range of 0.47 - 0.7 (Ergun 1952). These two models, combined with a transition point at a particle volume fraction of 0.2, can substantially cover the circulation flow. In addition, the sole use of Wen-Yu model may cause an overestimation in the prediction of drag force (Tu and Wang, 2018), which can be eliminated with the combined use of Wen-Yu and Ergun drag model to simulate the gas-solid two-phase flow. Wang *et al.* (2014a, 2014b) proved that the Wen-Yu/Ergun model was the optimal drag model to simulate a gas-solid two-phase flow in a cold fluidized bed. Extensive studies have used CPFD computational model and showed that the combined resistance model accurately predicted the flow characteristics in fluidized beds (Lan *et al.* 2013; Thapa *et al.* 2016; Zhang *et al.* 2012). The drag model is expressed using Eq. (7) – (9).

$$\theta_p > 0.85\theta_{cp} \quad C_d = D_2 \quad (7)$$

$$\theta_p < 0.75\theta_{cp} \quad C_d = D_1 \quad (8)$$

$$0.85\theta_{cp} \geq \theta_p \geq 0.75\theta_{cp}$$

$$C_d = \frac{\theta_p - 0.85\theta_{cp}}{0.85\theta_{cp} - 0.75\theta_{cp}} (D_2 - D_1) + D_1 \quad (9)$$

where D_1 is the Wen-Yu model drag force, and D_2 is the Ergun model drag force (D M Snider, 2001).

4. RESULTS AND DISCUSSION

4.1 Bubble Phenomenon

A comparison of the experimental test with the

numerical simulation is shown in Fig. 3. The three images show the experimental and simulation results for the same case, whereas the time interval of each image is 0.04 s. The comparison shows that the residence time of the bubbles was the same, and it took about 0.08s for the bubbles to disappear. The shape of the bubbles was relatively regular. There was a clear boundary between the bubbles and the particles. Based upon the conversion measurement of the same proportion, the ratios of the bubble diameter to radial length of the section in the three experimental images were 0.42, 0.3, and 0.38, whereas in the simulation results, the ratios of the bubble diameter to the radial length of the section were 0.45, 0.32, and 0.39. The experimental results agreed well with the simulation results and showed the motion trajectory of the bubbles. Apparently, the movement of air bubbles was preferentially straight along the vertical wall. Poor fluidization of particles was observed near the inclined wall. The aggregation of particles was spotted along the sloping wall, which will be further discussed in Section 4.2.

4.2 Particle Aggregation

According to the research of Cahyadi and Ananthara (2017), the characteristics of clusters are affected by many factors. It is worth noticing that the trend of cluster characteristics is relatively consistent. Therefore, there is no accurate benchmark data for the classification of particle agglomeration, which mainly depends on the scope and appearance of agglomeration. There were three types of particle aggregations in the fluidized bed: filamentous aggregation, flocculent aggregation and reunion aggregation. Filamentous aggregations are generally formed in low particle concentration zones, and particles are attached near the top boundary of large bubbles. When two or more filamentous agglomerates in a fluidized bed collide with each other and intertwine, flocculent particle aggregation will form. The reunion aggregation mainly refers to the phenomenon of particle agglomeration, in which the particle concentration and the agglomeration range in the fluidized bed exceed the former two.

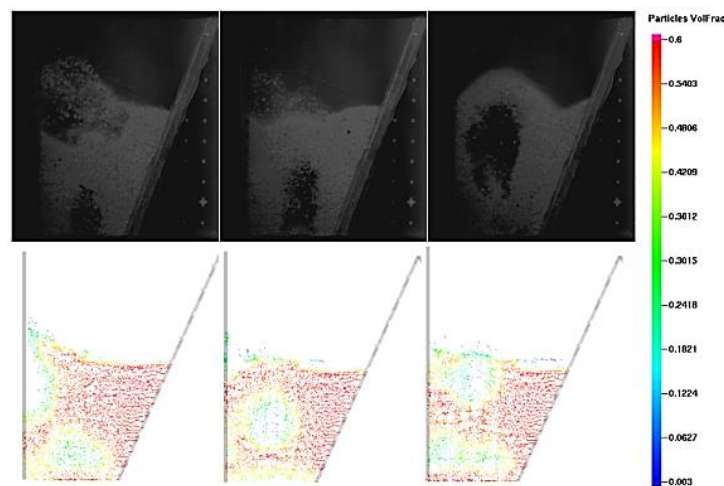


Fig. 3. Comparison of bubble phenomenon.

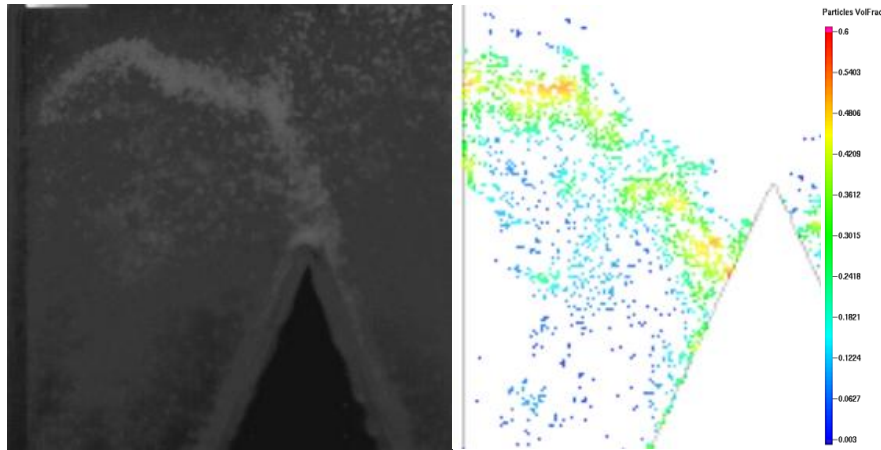


Fig. 4. Comparison of filamentous particle clusters ($h=20$ mm, $u_g=1.8$ m/s).

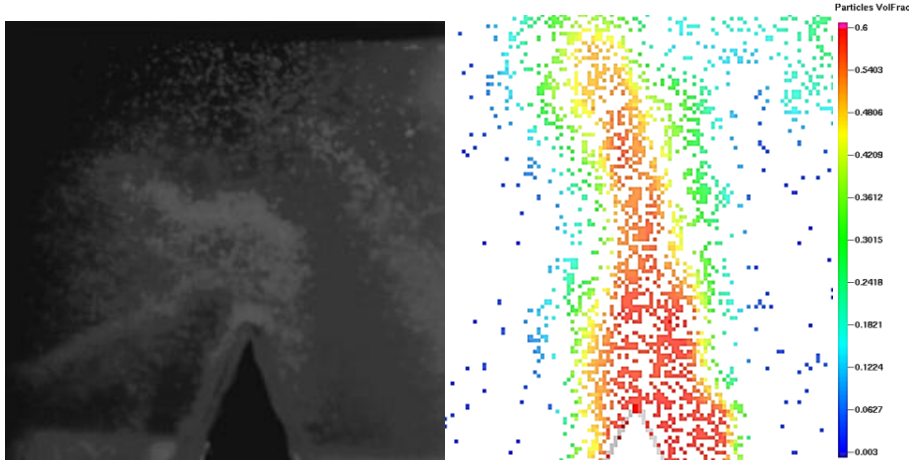


Fig. 5. Comparison of flocculent particle aggregation ($h=20$ mm, $u_g=1.8$ m/s).

4.2.1 Filamentous aggregation

Filamentous agglomeration refers to the existence of particle agglomerates with banded distribution, thin thickness and irregular trend. A comparison of the experimental and numerical simulations of the filamentous aggregation phenomenon is shown in Fig. 4. The filamentous particle clusters could be clearly seen from both the experimental and simulated results. The gas phase carried the particles to a certain height with a large number of particles attached to the front of large bubbles, and a thin layer of filamentous distribution appeared.

4.2.2 Flocculent aggregation

Flocculent agglomeration refers to the existence of several groups of filamentous particle agglomerates, which are intertwined with each other to form flocculent agglomeration. The results from an experiment and simulations to compare the flocculent aggregation phenomenon are shown in Fig. 5. The experimental results agreed well with the simulation results. The appearance of the flocculent clusters could be clearly displayed. In the upper particle migration zone, large bubbles generated on both the sides collided laterally, and the filamentous aggregates of the boundary layer of the large bubbles were intertwined to form a

flocculation cluster. The flocculent aggregation, similar to the filamentous aggregation, was relatively unstable. Due to the large internal voids of the flocculent aggregation, it was easy to be scattered when airflow entered. When the drag was small, it was easy to sink and form circulating particles.

4.2.3 Reunion aggregation

Reunion aggregation mainly refers to the phenomenon that the particle concentration and agglomeration range in the circulating fluidized bed exceed the first two. The comparison of the result of the aggregation phenomenon and the numerical simulation is shown in Fig. 6.

The position and the aggregation range of the cluster-like aggregates mainly appeared along the inclined wall. In the fluidized bed, due to the existence of inclined wall, when the particles flowed down the inclined wall, the flow area on the side of the inclined wall gradually became smaller, resulting in uneven pressure distribution on the bed. As a result, more particles accumulated on the wall, forming particle aggregation. The particles accumulated more at this site, thereby forming reunion aggregation. Since the particles were significantly aggregated in the aggregation range

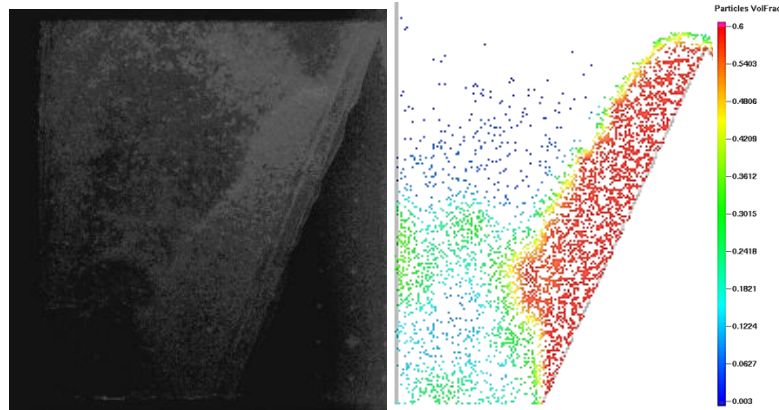


Fig. 6. Comparison of mass aggregation ($h=55$ mm, $u_g=3.5$ m/s).

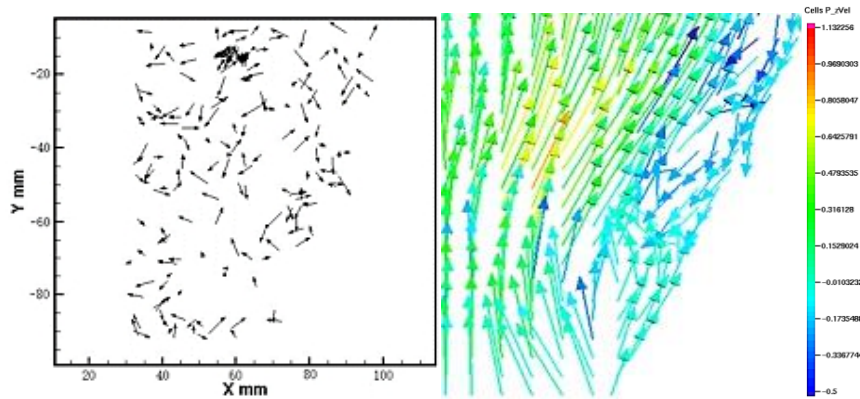


Fig. 7. Particle velocity vector comparison.

and the particles' concentration was higher than the former two particles' aggregations, the particle aggregation had a relatively stable morphology.

4.2.4 Comparison of flow characteristics in the dense phase region

The comparison of particle velocity vector in the dense phase region is shown in Fig. 7. In the leg, the movement of particles was random and the flow was disorderly. This was because, the particles were affected by the upward drag force due to air flow, the inertial force of their own falling and the force between the particles. The results of the experiment and the simulation showed that the particles formed local swirl around the inclined wall. Due to the existence of inclined wall, the particles flowed downwards along the inclined wall, forming a clockwise flow structure. It could be clearly seen from the simulation results that due to the existence of inclined wall, some particles were carried by the airflow to deflect to the vertical wall first, and then, to the inclined wall with the increase of the flow area.

4.3 Gas-solid Flow Characteristics in the Dense Phase Region

4.3.1 Flow analysis of dense phase region without secondary air

Figure 8 shows a distribution diagram of the particle volume fraction at the dense phase region without secondary air within 1 s. Time increment between each case was 0.1 s.

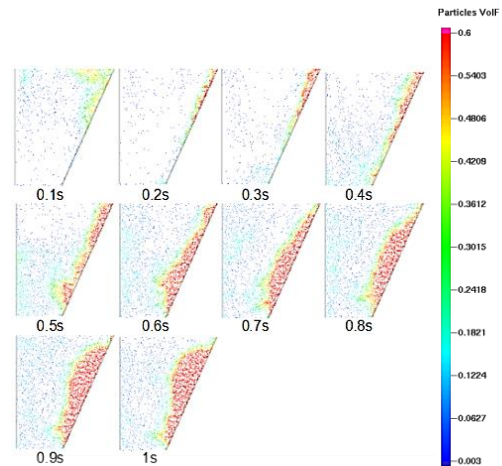


Fig. 8. Distribution of the particles' volume fraction.

At the initial 0.1 s, when air entered the fluidized bed from the bottom, the particles were carried to a certain height, and a bubble-like structure was formed due to the scouring of the air current. Meanwhile, the concentration of sand in the dense phase region was the lowest. After that, many circulating particles gradually flowed back to the side walls. The concentration of the particles around the inclined wall was much higher than that along the vertical wall. This was because, the flow area on the side of the inclined wall gradually decreased when the particles flowed down the inclined wall. It

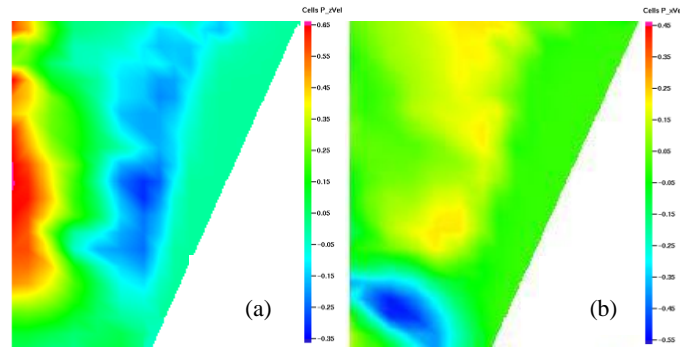


Fig. 9. Particle velocity distribution. (a) Axial velocity distribution. (b) Radial velocity distribution.

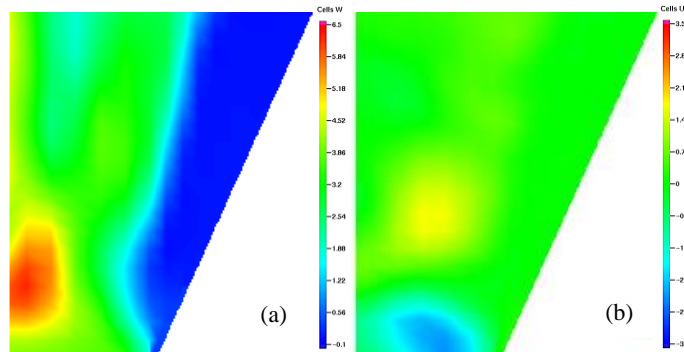


Fig. 10. Particles' volume fraction distribution.

caused a large number of particles to aggregate, due to which, more particles accumulated in this zone, forming particle aggregation. When the fluidization time reached 0.8 s, a relatively stable aggregated particle mass was formed on the inclined wall's surface. An asymmetric distribution of particle concentrations was created in the radial direction.

Figure 9 shows the distributions of axial and radial velocities of the particles in the dense phase region at 1 s fluidization time. The particles formed a circular flow pattern in the dense phase of the fluidized bed, and the vertical wall's side wall area did not form a descending particle group with a higher concentration. However, it formed a particle group that moved up quickly. The particles had a clockwise flow structure in the left leg. The rising speed of the particles was greater than the falling speed. However, the aggregated particle clusters, accumulated on the inclined wall's surface, were hardly subjected to primary air purging, and the axial and radial velocities of the particles inside the particle cluster were small. Moreover, only the particles on the surface of the pellets participated in the circulation of particles.

Figure 10 shows the gas axial velocity distribution and radial velocity distribution in the dense phase region when the fluidization time is 1 s. Due to the influence of the accumulation of sloping wall particles, the gas was deflected towards the vertical wall, followed by deflection towards the inclined wall. Since the inclined wall was a slope, a large amount of particle aggregation occurred on the inclined wall's surface, and the aggregation range and particle concentration were large, resulting in a

small velocity of the gas particles flowing through the inclined wall's surface.

Some studies (W. Chan *et al.*, 2010; Xu and Zhu, 2011) have indicated that the formation of particle aggregation in the core-annulus structure may have been caused by the wall effect. The gas phase velocity in the area near the wall decreased, and resulted in the slowing down of particle velocity, finally forming particle aggregation. This was consistent with the simulation results.

It can be observed that, in the case of only primary air, the particles' aggregation phenomenon was formed, which was not conducive to fluidization. Many works (Kim and Shakourzadeh, 2000; Koksai and Hamdullahpur, 2004; Lv *et al.*, 2020; Zheng *et al.* 2019) have pointed out that the addition of secondary air can effectively improve the fluidization of particles. Based on the theories of these works, this study will predict the influence of secondary air on particles' aggregation.

4.3.2 Influence of secondary air on the particle flow of dense phase region

Figure 11 is a comparison of particles' volume fraction distribution in the dense phase region with or without secondary air.

The static bed material height was 30 mm and the gas flow rate in one leg was 5.5 m³/h. When there was no secondary air, the primary air velocity was 3.5 m/s. After the secondary air was added, the primary air velocity was 3 m/s and the secondary air velocity was 5 m/s. The results show that the particles' volume fraction distribution in the dense phase of the fluidized bed was greatly improved by

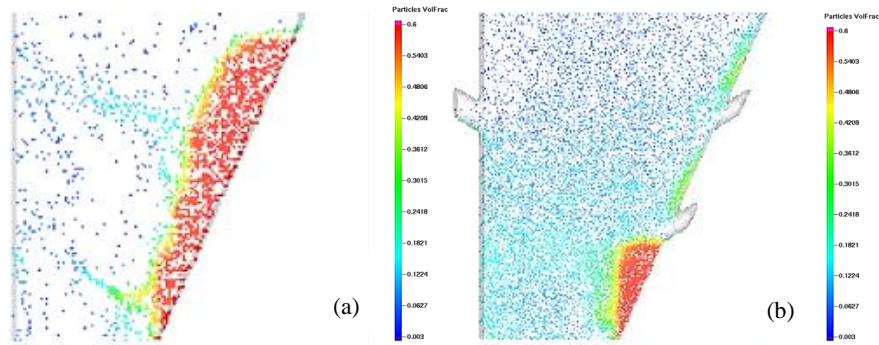


Fig. 11. Comparison of particles' volume fraction distribution. (a) Case without the secondary air. (b) Case with the secondary air.

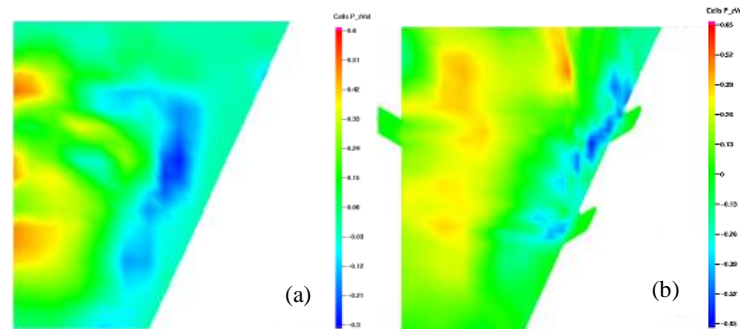


Fig. 12. Comparison of the distribution of axial velocity of particles. (a) Case without the secondary air. (b) Case with the secondary air.

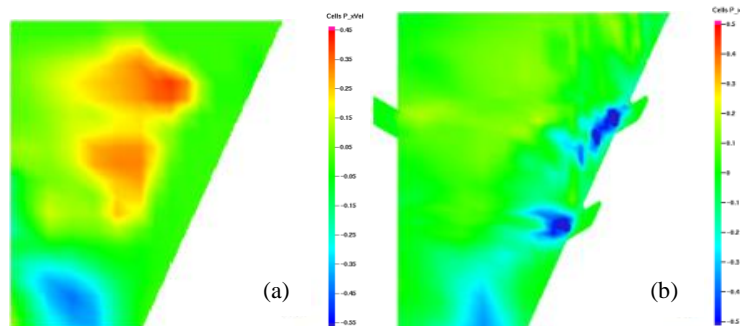


Fig. 13. Comparison of the distribution of radial velocity of particles. (a) Case without the secondary air. (b) Case with the secondary air.

the secondary air. The addition of secondary air effectively reduced the accumulation of particles on the surface of the inclined wall, and formed a high concentration of particles at the lower part of the inclined wall. This made the particles' volume concentration distribution more uniform in the radial direction, which proved that the addition of secondary air in the dense phase region could effectively promote the radial mixing of the particles. The secondary air had different effects on the particle concentration at different heights. The particle concentration was higher in the area below the secondary air outlet, while it was lower in the area above the secondary air outlet. This effect was believed due to the shearing and obstructing effects of the secondary air jet during the upward movement of the gas-solid flow in the furnace. For a constant total volume of the fluidized air, when the secondary air was added, the primary air volume was correspondingly reduced. Under the combined

effects of downward secondary air jet and reduced velocity of primary air, more bed material was suppressed below the secondary air outlet, and the particle concentration in the legs gradually decreased with the increase in height.

Figure 12 shows the distributions of axial and radial velocities of the dense phase zone without secondary air. Fig. 13 shows the distributions of axial and radial velocities of the dense phase region with secondary air. The addition of secondary air had an obvious influence on the gas-solid two-phase flow in the dense phase region, and different axial positions were affected by the secondary air. The addition of secondary air mainly changed the gas-solid flow distribution in the inclined wall zone. When there was no secondary air in the dense phase region, the velocity of the particles on the inclined wall surface was small. When the secondary air jet was injected obliquely downwards into the leg at 30° from the horizontal direction, the particles at the

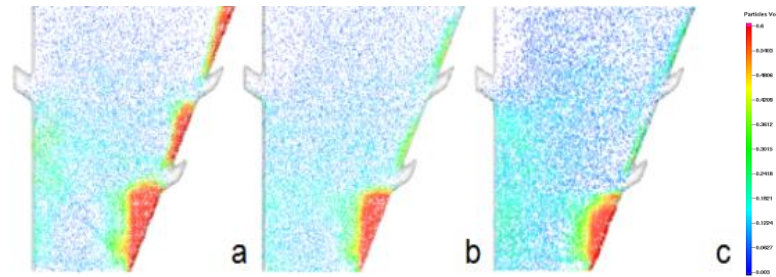


Fig. 14. Comparison of the distribution of the volume fraction of particles. (a) When secondary air velocity was 4 m/s. (b) When secondary air velocity was 5 m/s. (c) When secondary air velocity was 6 m/s.

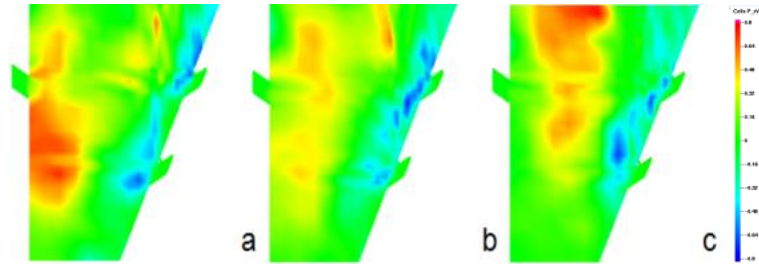


Fig. 15. Comparison of the distribution of particles' axial velocity. (a) When secondary air velocity was 4 m/s. (b) When secondary air velocity was 5 m/s. (c) When secondary air velocity was 6 m/s.

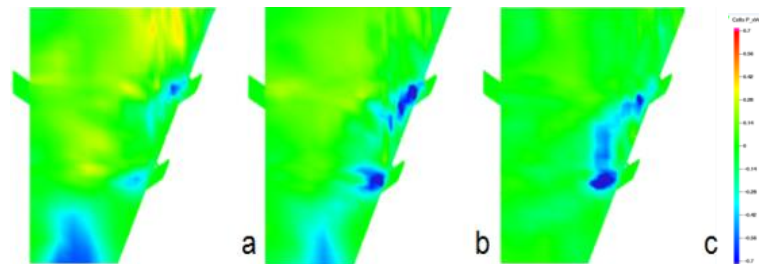


Fig. 16. Comparison of the distribution of particles' radial velocity. (a) When secondary air velocity was 4 m/s. (b) When secondary air velocity was 5 m/s. (c) When secondary air velocity was 6 m/s.

secondary air outlet of the inclined wall were subjected to gas-phase entrainment, and the axial and radial velocities rapidly increased. However, because the secondary air of the inclined wall was impacted by the high-concentration downward-flow, the secondary air of the vertical wall was strongly affected by the primary air, and the energy dissipation was faster. In the left leg, the particles were in a clockwise circulatory flow structure. After the addition of the secondary air, the particles formed a small partial clockwise circulation flow in the area above the secondary air vent of the inclined wall. Because the increase of the fluidized air volume was greater than the increase in the cross-sectional area of the furnace, the velocity of the upward movement of the particles above the secondary air outlet increased.

4.3.3 Effect of secondary air velocity on flow in the dense phase region

Figure 14 shows the distribution of the volume fraction of particles of the dense phase region at different secondary air velocities. The static bed height was 30 mm, whereas the primary air velocity was 3 m/s. Moreover, the secondary air velocities were varied through values of 4 m/s, 5 m/s and 6

m/s. The increase in the secondary air velocity promoted more uniform distribution of the particle concentration in the radial direction. As the velocity increased, the lateral impact on the primary air got enhanced, causing the partially moving particles to change the flow direction from the side wall zone to the central zone, so that the particles were concentrated in the central zone of the dense phase region. The phenomenon intensified as the secondary air velocity increased. The accumulation volume of the particle group at the bottom of the inclined wall surface was reduced, and the hindrance effect of the secondary air jet was strengthened. Therefore, more bed material was suppressed below the secondary air outlet, due to which, the particle concentration in the lower part of the furnace increased. When the velocity reached 5 m/s, the particles would only accumulate at the bottom of the inclined wall, and the boundary layer thickness and the particle concentration of the falling wall of the inclined wall decreased with the increase of the secondary air velocity.

Figures 15 and 16 show the axial and radial velocity profiles of the particles in the dense phase region at different secondary air velocities, respectively.

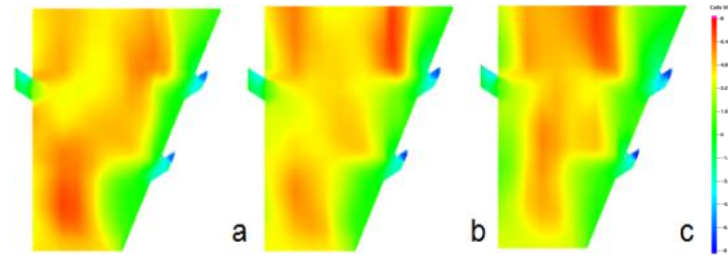


Fig. 17. Comparison of the distribution of the axial velocity of gas. (a) When secondary air velocity was 4 m/s. (b) When secondary air velocity was 5 m/s. (c) When secondary air velocity was 6 m/s.

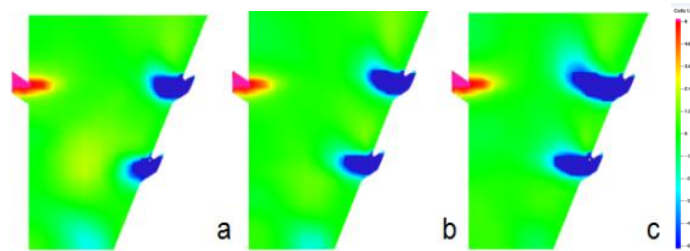


Fig. 18. Comparison of the distribution of the radial velocity of gas. (a) When secondary air velocity was 4 m/s. (b) When secondary air velocity was 5 m/s. (c) When secondary air velocity was 6 m/s.

When the secondary air velocity increased, the air velocity of the empty section increased, due to which, the axial and radial velocities of the particles increased. Meanwhile, the height of the maximum rising velocity of the particles also increased. Because the secondary air injection had the effect of shearing and obstructing the upward movement of gas and solid particles in the furnace, the radial velocity of the particles in the bottom zone of the dense phase region and above the secondary air outlet decreased with the increase of velocity.

Figures 17 and 18 show the axial and radial velocity distributions of the gas in the dense phase region at different secondary air velocities, respectively. At the same time, particles moved under the actions of drag force of upward air flow, inertial force of particles and the force between the particles, and there was a certain lag between the movement speed of particles and the change of gas velocity in this area. Due to these reasons, the particle velocity at the secondary air outlet could not accurately reflect the penetration depth of secondary air. The radial velocity of the gas reflected the flow of gas in the zone, and the jet depth of the secondary air could be more accurately reflected. When the secondary air jet entered the dense phase zone obliquely downwards at 30° from the horizontal direction, it will diffuse simultaneously in the radial and axial directions. The surrounding gas and solid particles hindered the jet depth of the secondary air through collisions and entrainment, so that the velocity of the jet was continuously attenuated throughout the process. The depth of the secondary air jet increased with the increase of the secondary air velocity. When the secondary air velocity reached 6 m/s, the secondary air could basically penetrate half of the legs. As the secondary air velocity increased, the shearing and obstruction of the secondary air jet to the upward gas-solid flow in the furnace also increased, leading to a reduction in the axial velocity of the gas in the wall zone above

the secondary air outlet of the vertical wall. Since the primary air had a significant influence on the secondary air purging of the vertical wall, the penetration depth of the secondary wall of the vertical wall was small. The addition of the secondary air caused the gas velocity of the section to increase, and the axial velocity of the gas above the secondary air outlet increased significantly.

It can be observed from the results that the addition of secondary air made the particle distribution more uniform, and different secondary air velocities had significant effects on the particles' distribution in the dense phase zone. The distribution of solid-gas flow in the region became more evenly with higher secondary air velocities within the range of 4 - 6 m/s. Therefore, when considering the secondary air parameters in design, properly increasing the secondary air speed could promote the particle mixing.

5. CONCLUSIONS

In this study, the two-dimensional cold state test bed of fluidized bed was built and the numerical simulation method was used to study the impact of secondary air on the gas-solid flow in the dense phase of the fluidized bed. From the results of experiments and simulations, the bubble behavior test results were found to be in good agreement with the simulation results. The motion of the bubbles was determined. The phenomenon of particle aggregation in the test and simulation clearly showed the morphology, appearance and the appearance of filamentous and flocculent lumps. However, due to the existence of inclined wall, a partial swirl phenomenon occurred on the inclined wall surface.

In the dense phase region without secondary air, only the particles on the surface of the particle group participated in the flow of the particles. The

particles' volume fraction near the vertical wall of the leg was about 12% and the volume fraction of particles near the inclined wall of the leg was about 54%, with a difference of 42%, which resulted in an asymmetric distribution of particle concentration along the radial direction. With the introduction of secondary air, the distribution of particles along the radial direction was significantly improved. Moreover, the difference between the volume fraction of the particles near the vertical and inclined walls was narrowed from 42% to 13%, indicating that the proper arrangement of secondary air could effectively promote the mixing of particles in the pant-leg section.

The secondary air had different degrees of effects on the particle concentration at different heights. The particle concentration in the area above the secondary air outlet was small, and the particle concentration in the area below the secondary air outlet was large. As the secondary air velocity increased from 4 m/s to 6 m/s, the partially moving particles changed the flow direction due to the lateral impact of the primary air, and accumulated in the central zone. Due to this reason, the particle concentration in the central zone of the dense phase region increased. The accumulation volume of the particle group at the bottom of the inclined wall's surface reduced, whereas the hindrance effect of the secondary air jet strengthened, due to which, more bed material was suppressed below the secondary air outlet, and the particle concentration in the lower part of the furnace increased.

Based on the results, it can be inferred that, when designing the secondary air parameters of the fluidized bed, proper adjustment of the secondary air velocity can have a positive effect on particle mixing.

ACKNOWLEDGEMENTS

This study was supported by the Jilin Science and technology innovation development plan (20210103091).

REFERENCES

Abbasi, A., P. E. Ege and H. I. De Lasa (2011). CPFD simulation of a fast fluidized bed steam coal gasifier feeding section. *Chemical Engineering Journal* 174(1), 341–350.

Atsonios, K., A. Nikolopoulos, S. Karellas, N. Nikolopoulos, P. Grammelis and E. Kakaras (2011). Numerical investigation of the grid spatial resolution and the anisotropic character of EMMS in CFB multiphase flow. *Chemical Engineering Science* 66(17), 3979–3990.

Auzerais, F. M., R. Jackson and W. B. Russel (1988). The resolution of shocks and the effects of compressible sediments in transient settling. *Journal of Fluid Mechanics* 195, 437–462.

Basu, P. (2015). Circulating fluidized bed boilers, design operation and

maintenance. *Springer International Publishing Switzerland*.

Cahyadi, A. and A. Anantharaman (2017). Review of cluster characteristics in circulating fluidized bed (CFB) risers. *Chemical Engineering Science* 158, 70–95.

Chan, C. W., J. P. K. Seville, D. J. Parker and J. Baeyens (2010). Particle velocities and their residence time distribution in the riser of a CFB. *Powder Technology* 203(2), 187–197.

Chen, C., J. Werther, S. Heinrich, H. Y. Qi and E.-U. Hartge (2013). CPFD simulation of circulating fluidized bed risers. *Powder Technology* 235, 238–247.

CPFD Software (2015). *Barracuda Virtual Reactor User Manual*. USA: CPFD Software LLC.

Cui, Y. and W. Q. Zhong (2021). Study on scale-up characteristics in supercritical CO₂ circulating fluidized bed boiler by 3D CFD simulation. *Powder Technology* 394, 103–119.

Cundall, P. A. and O. D. L. Strack (1979). A discrete numerical model for granular assemblies. *Geotechnique* 29(1), 47–65.

Ergun, S. (1952). Fluid flow through packed columns. *Journal of Materials Science and Chemical Engineering* 48, 89–94.

Gao, J., J. Chang, C. Lu and C. Xu (2008). Experimental and computational studies on flow behavior of gas–solid fluidized bed with disparately sized binary particles. *Particuology* 6(2), 59–71.

Godlieb, W., N. G. Deen and J. A. M. Kuipers (2007). A discrete particle simulation study of solids mixing in a pressurized fluidized bed. *Proceedings of the 12th International Conference On Fluidization : New Horizons in Fluidization Engineering* 92, 751–758.

Grace, J. R. and G. Sun (1991). Influence of particle size distribution on the performance of fluidized bed reactors. *The Canadian Journal of Chemical Engineering* 69(5), 1126–1134.

Hartge, E. U., L. Ratschow, R. Wischnewski and J. Werther (2009). CFD-simulation of a circulating fluidized bed riser. *Particuology* 7(4), 283–296.

Jenkins, J. T. and F. Mancini (1989). Kinetic theory for binary mixtures of smooth, nearly elastic spheres. *Physics of Fluids A: Fluid Dynamics* 1(12), 2050–2057.

Kim, J. H. and K. Shakourzadeh (2000). Analysis and modelling of solid flow in a closed loop circulating fluidized bed with secondary air injection. *Powder Technology* 111(3), 179–185.

Kleinstreuer, C. (2003). Two-phase flow: theory and applications. *CRC Press*.

Koksal, M. and F. Hamdullahpur (2004). Gas Mixing in Circulating Fluidized Beds with Secondary Air Injection. *Chemical*

- Engineering Research and Design* 82(8), 979–992.
- Lan, X., X. Shi, Y. Zhang, Y. Wang, C. Xu and J. Gao (2013). Solids back-mixing behavior and effect of the mesoscale structure in CFB risers. *Industrial & Engineering Chemistry Research* 52(34), 11888–11896.
- Liu, H., J. Li and Q. Wang (2017). Simulation of gas–solid flow characteristics in a circulating fluidized bed based on a computational particle fluid dynamics model. *Powder Technology* 321, 132–142.
- Lv, B., Z. Luo, X. Deng, J. Chen, C. Fang and X. Zhu (2020). Hydrodynamics and subsequent separation of gas-solid separation fluidized bed with secondary air injection. *Powder Technology* 366, 197–205.
- Nardo, A. D., G. Calchetti and S. Stendardo (2018). Modeling and Simulation of an Oxygen-Blown Bubbling Fluidized Bed Gasifier using the Computational Particle Fluid Dynamics (CPFD) Approach. *Journal of Applied Fluid Mechanics* 11(4), 825–834.
- O'Rourke, P. J. (1981). Collective drop effects on vaporizing liquid sprays. *Los Alamos National Lab., NM (USA)*.
- Qiu, G., J. Ye and H. Wang (2015). Investigation of gas–solids flow characteristics in a circulating fluidized bed with annular combustion chamber by pressure measurements and CPFD simulation. *Chemical Engineering Science* 134, 433–447.
- Raheem, D. G., B. Yilmaz and S. Özdoğan (2019). Cold Flow Simulation of a 30 kWth CFB Riser with CPFD. *Journal of Applied Fluid Mechanics* 13(2), 603–614.
- Shi, X., R. Sun, X. Lan, F. Liu, Y. Zhang and J. Gao (2015). CPFD simulation of solids residence time and back-mixing in CFB risers. *Powder Technology* 271, 16–25.
- Shi, X., X. Lan, F. Liu, Y. Zhang and J. Gao (2014). Effect of particle size distribution on hydrodynamics and solids back-mixing in CFB risers using CPFD simulation. *Powder Technology* 266, 135–143.
- Snider, D. M. (2001). An incompressible three-dimensional multiphase particle-in-cell model for dense particle flows. *Journal of Computational Physics* 170(2), 523–549.
- Snider, D. M., P. J. O'Rourke and M. J. Andrews (1998). Sediment flow in inclined vessels calculated using a multiphase particle-in-cell model for dense particle flows. *International Journal of Multiphase Flow* 24(8), 1359–1382.
- Snider, M. Dale, S. M. Clark and P. J. O'Rourke (2011). Eulerian–Lagrangian method for three-dimensional thermal reacting flow with application to coal gasifiers. *Chemical Engineering Science* 66(6), 1285–1295.
- Thapa, R. K., A. Frohner, G. Tondl, C. Pfeifer and B. M. Halvorsen (2016). Circulating fluidized bed combustion reactor: Computational Particle Fluid Dynamic model validation and gas feed position optimization. *Computers & Chemical Engineering* 92, 180–188.
- Tu, Q. and H. Wang (2018). CPFD study of a full-loop three-dimensional pilot-scale circulating fluidized bed based on EMMS drag model. *Powder Technology* 323, 534–547.
- Tu, Q. and Z. Luo (2021). MP-PIC simulation of the gas-solid full-loop flow characteristics in a dual fluidized bed and validation with experimental data. *Chemical Engineering Journal* 421, 129835.
- Wang, Q., H. Yang, P. Wang, J. Lu, Q. Liu, H. Zhang, L. Wei and M. Zhang (2014a). Application of CPFD method in the simulation of a circulating fluidized bed with a loop seal, part I—Determination of modeling parameters. *Powder Technology* 253, 814–821.
- Wang, Q., H. Yang, P. Wang, J. Lu, Q. Liu, H. Zhang, L. Wei and M. Zhang (2014b). Application of CPFD method in the simulation of a circulating fluidized bed with a loop seal Part II—Investigation of solids circulation. *Powder Technology* 253, 822–828.
- Wen, C. and Y. Yu (1966). Mechanics of fluidization. *Chemical Engineering Progress Symposium Series* 62(62), 100–111.
- Xu, J. and J. X. Zhu (2011). Visualization of particle aggregation and effects of particle properties on cluster characteristics in a CFB riser. *Chemical Engineering Journal* 168(1), 376–389.
- Yan, J., X. F. Lu and R. Xue (2020). Validation and application of CPFD model in simulating gas-solid flow and combustion of a supercritical CFB boiler with improved inlet boundary conditions. *Fuel Processing Technology* 208, 106512.
- Yeoh, G. H. and J. Tu (2019). *Computational techniques for multiphase flows*. Butterworth-Heinemann.
- Zhang, H. D. and W. B. Li (2020). Numerical study on influence of exit geometry in gas - solid flow hydrodynamics of HDCFB riser by CPFD. *Advanced Powder Technology* 31, 4005–4017.
- Zhang, Y., X. Lan and J. Gao (2012). Modeling of gas-solid flow in a CFB riser based on computational particle fluid dynamics. *Petroleum Science* 9(4), 535–543.
- Zheng, W., M. Zhang, Y. Zhang, J. Lyu and H. Yang (2019). The effect of the secondary air injection on the gas–solid flow characteristics in the circulating fluidized bed. *Chemical Engineering Research and Design* 141, 220–228.